Rawafed Almarefa Journal مجلة روافد المعرفة
ISSN: 2709-0345 Volume: 6, Issue: 12, June (2026), Pages: 164-187

Physical Evaluation of Atmospheric Optical Properties and Solar Radiation Analysis over Tarhuna – Libya by using NASA POWER Data

Nagia Ali Abdurahim Abussif

Department of Physics, Faculty of Science, Azzaytuna University, Libya

najea781418@gmail.com

Received:10.-05-2026; Accepted:20.05-2026; Published: 06-06-2026

Abstract

This study presents a physical evaluation of atmospheric optical properties and solar radiation parameters over Tarhuna, Libya$(32.430\,N\,,13.630\,E)$, (398 m, above sea level) by using resolutions daily for the year 2025. Given the lack of local ground based meteorological stations in Tarhuna, daily global horizontal irradiance (H) was sourced from the NASA POWER database. To assess the atmospheric conditions, the Erbs decomposition model was applied to partition the global radiation into its direct and diffuse components. This mathematical approach was chosen because it delivers reliable data for solar energy applications, overcoming the high margins of error that are typically associated with raw satellite observations. The direct horizontal component(H_b) was converted into direct normal irradiation (DNI) using the solar zenith angle (θ_z) while the atmospheric optical depth (τ) was derived by the Beer-Lambert law as a function of solar noon air mass(AM_{noon}). The statistical and optical results showed that the atmosphere reached its highest levels of clarity and stability in summer. July recorded the lowest daily variance $(Cv\,\% = 2.77\%)$, $(SD = 0.2243)$ due to clear skies, resulting in positive findings in contrast, seasonal shifts caused disturbances in the optical properties. In April, desert dust storms shift the atmospheric transmission into a Mie scattering regime, pushing the atmospheric optical depth to its annual peak $(\tau = 0.298)$ and reducing direct solar irradiance (DNI) to its minimum (2.5 kWh/m^2/ day). However, global horizontal irradiance (H) remains high (6.7617 kWh/m^2/ day) because large dust particles scatter light downward as diffuse horizontal irradiation (DHI), a phenomenon further amplified by multiple scattering with the Earth's surface. In November, autumn rains effectively washed aerosols from the atmosphere, reducing the optical depth to its annual minimum $(\tau = 0.212)$ and raising the clearness index to its peak $(K_t = 0.6773)$, where molecular Rayleigh scattering of clear air domineer. dominates Daily resolution Pearson correlation matrix analysis revealed a near-perfect inverse relationship between (K_t) and (τ) $(r = -0.9782)$ and a strong negative correlation between (DNI) and (τ) ($r = -0.8412$). The correlation between (DNI) and (K_t) was found to be ($r = +0.7645$), the non-perfect linearity of this specific relationship is physically explained by dust storms converting direct radiation into diffuse radiation. In conclusion ,this study provides a basic framework for solar energy projects and optical properties of the atmosphere in the study area ,where the annual average global horizontal irradiance of (5.7239 kWh/m^2/day) accompanied by annual clearness index of (K_t = 0.6006).

Keywords: Solar Radiation, Atmospheric Optical Properties, NASA POWER, Tarhuna, Libya, Clearness Index, Air Mass , Optical Depth

الملخص

يقدم هذا البحث تقييما فيزيائياً للخصائص البصرية للغلاف الجوي وتحليلاً للإشعاع الشمسي في ترهونة بليبيا (32.43 شمالاً، 13.63 شرقاً) وارتفاع (398 متراً عن سطح البحر) ، وذلك باستخدام البيانات اليومية لعام 2025 والمستخرجة من قاعدة بيانات (NASA POWER)، ونظراً لعدم توفر محطات أرصاد جوية ارضية في منطقة ترهونة، تم اعتماد بيانات الإشعاع الأفقي الكلي (H) من ناسا، ولحساب الاشعاع العمودي المباشر (DNI) تم استخدام نموذج " إربس" (Erbs) لفصل الإشعاع الكلي إلى مكوناته المباشر و المنتشر، حيث جرى الاعتماد على نموذج الفصل لأن نماذج فصل الإشعاع تعطي نتائج أكثر ملاءمة للتطبيقات الشمسية مقارنة بالبيانات الجاهزة المستمدة من الأقمار الصناعية والتي تعاني من هوامش خطأ مرتفعة في قيم الإشعاع المباشر (DNI) على عكس قيم الإشعاع الكلي. بعد ذلك تم تحويل الإشعاع المباشر الافقي الى اشعاع عمودي مباشر (DNI) باستخدام زاوية السمت الشمسية (θ_Z) وفي الخطوة الأخيرة، تم حساب العمق البصري للغلاف الجوي (τ) بتطبيق قانون "بير-لامبرت" كدالة في كتلة الهواء عند الظهر (AM_{noon}). أظهرت النتائج الاحصائية أن الاشعاع الشمسي يكون مستقراً للغاية ويمكن التنبؤ به خلال فصل الصيف، حيث سجل شهر يوليو اقل تباين يومي على مدار السنة (Cv % =2.77) و (SD=0.2243) نتيجة لصفاء السماء المستمر، في المقابل يظهر فصل الربيع عكارة جوية عالية، ففي شهر أبريل، تؤدي العواصف الترابية الصحراوية إلى رفع العمق البصري للجو إلى أعلى قيمة سنوية ($\tau = 0.298$) ويسبب هذا الغبار في حدوث تشتت "ميه" (Mie scattering) مما يخفض شدة الإشعاع المباشر (DNI) الى ادنى مستوياته البالغة (2.5 KWh/m^2/day) ومع ذلك ، يلاحظ أن الإشعاع الأفقي الكلي (H) يظل مرتفعاً عند (6.717 KWh/m^2/day) لأن حبيبات الغبار الكبيرة تسبب في تشتت الاشعة نحو الاسفل ليصل إلى الأرض كإشعاع منتشر (DHI)، ويساعد في ذلك ايضاً حدوث تشتت متعدد للأشعة بين الجو المحمل بالتراب وسطح الأرض، أما في شهر نوفمبر فإن أمطار الخريف تغسل الغبار تماماً من السماء، مما يخفض العمق البصري إلى أدنى قيمة سنوية له ($\tau = 0.212$) ويرفع مؤشر الصفاء إلى اقصى قيمة له (K_t =0.6773) تحت سيطرة تشتت " ريلي" (Rayleigh scattering) الضعيف والمستقر المميز لجزيئات الهواء النقي. أكد تحليل ارتباط " بيرسون" المعتمد على البيانات اليومية وجود علاقة عكسية قوية جداً بين مؤشر الصفاء والعمق البصري للجو ($r = -0.9782$) ، وعلاقة عكسية قوية بين الإشعاع المباشر والعمق البصري ($r = -0.8912$) كما بلغت قيمة معامل الارتباط بين الإشعاع المباشر ومؤشر الصفاء ($r = +0.7645$) ، ويفسر عدم وصول هذه العلاقة إلى الخطية المثالية فيزيائياً لقيام العواصف الترابية بتحويل اشعة الشمس المباشرة إلى منتشرة. توفر هذه الدراسة إطاراً اساسياً لمشاريع الطاقة الشمسية ودراسة الخصائص البصرية للغلاف الجوي في منطقة الدراسة والتي يسجل فيها المتوسط السنوي الإشعاع الأفقي العالمي معدل (5.7234 KWh/m^2/day) مصحوباً بمؤشر صفاء K_t =0.6006.

الكلمات المفتاحية: الإشعاع الشمسي، الخصائص البصرية للغلاف الجوي، ناسا POWER، ترهونة، ليبيا، مؤشر الوضوح، كتلة الهواء، العمق البصري.

1 INTRODUCTION

Solar radiation is the main energy source reaching the Earth**,** driving the physical processes underlying climate change and surface energy balance (Iqbal, 1983). These electromagnetic waves travel from the sun through space, carrying energy across the ultraviolet (UV), visible light, and infrared (IR) spectra. This energy plays a key role in atmospheric heating, surface energy balance, and the initiation of physical processes (Liou, 2002). Before reaching the ground, solar radiation interacts with the Earth's atmosphere, where gases, aerosols, clouds, and the ozone layer absorb and scatter a portion of it, lowering its overall intensity (Liou 2002, Wallace and Hobbs 2006). The geometric and physical factors directly control the amount of radiation that reaches the surface. Among these variables, the solar declination angle (δ) and the solar zenith angle (θ_Z) are important because they control the sun's position relative to the surface throughout the year (Liou, 2002). Owing to the tilt of the Earth's axis, the sun's angular deviation north or south of the equator changes with the seasons. This tilt causes variations in solar radiation intensity, which shapes the distribution of solar energy across the planet (Ahwida et al., 2013).

Zenith angle: The angle between the vertical line and the path of the sun's rays directly affects the intensity of solar radiation falling on a horizontal surface. As the zenith angle increases, the radiation intensity decreases because the rays travel farther through the atmosphere and spread over a wider area, causing more absorption and scattering along the path length (Wallace & Hobbs, 2006). Outside the Earth's atmosphere, at the average distance between the Earth and the sun, the solar constant represents the solar radiative power incident perpendicular to a unit area (Duffie & Beckman, 2013). Once solar radiation penetrates the atmosphere, it is split into direct and indirect components. The sun angle, atmospheric clarity, and obstacles such as clouds and topography strongly influence this path (Liou 2002). Indirect radiation, which comes from sunlight scattering in all directions, is highly sensitive to these atmospheric factors, and the sum of direct and indirect radiation forms the total global solar radiation (TGS).

To measure how the atmosphere alters this intensity, the atmospheric clearness index (K_t) serves as a physical tool to check clarity. It represents the ratio of solar radiation recorded at the Earth's surface to the solar radiation above the atmosphere under clear sky conditions. Researchers frequently use the clearness index to track fluctuations in solar radiation under various local weather conditions, as it reflects the combined effects of water vapor, aerosols, and atmospheric gases. Ultimately, this parameter offers a reliable basis for evaluating the atmospheric transparency (Duffie & Beckman, 2013).The solar radiation reaching the surface depends on the air mass (AM) which represents the optical path through the atmosphere (Petty 2006), the atmospheric optical depth (τ) which shows how much radiation is absorbed and scattered by dust, gases, and aerosols.

Several studies have examined solar radiation characteristics and physical analyses focusing on global solar radiation, and investigated the optical properties of the atmosphere in different cities, focusing on parameters such as the clearness index, aerosol optical depth, and scattering properties. Some of these studies relied on data from the NASA POWER project.

Teyabeen et al. (2024) evaluated the monthly global solar radiation in 12 major Libyan cities. This study analyzed regression methods and identified suitable empirical models for the Libyan climate. While, Mohamed et al. (2013) explored the relationship between the daily diffuse fraction and the clearness index (K_t) across three distinct climatic regions in Libya: Sabha (desert), Ghadames (semi-arid), and Tripoli (Mediterranean) . This study established a correlation for the average daily diffuse fraction and compared it with several global models, such as those of Liu and Jordan, and Erbs.

Abdulraheem and Omar (2024) performed a statistical analysis of global solar radiation and climatic parameters for Libyan cities and compared solar data with weather factors, such as relative humidity. Campanelli et al. (2022) analyzed aerosol optical properties in Rome, Italy, over an 11-year period, finding that aerosol optical depth and single scattering albedo significantly affected surface solar radiation, which underscores the importance of aerosols in modulating atmospheric optical properties. Similarly, Orte et al. (2021) compared NASA POWER solar radiation data with ground measurements in southern South America and found a high agreement $(R^2 \geq 0.95)$ confirming the reliability of NASA POWER data for solar radiation studies. Quansah et al. (2022) also validated NASA POWER satellite based Global Solar Radiation (G) data across 22 synoptic stations in Ghana by comparing it with sunshine duration measurements, noting that bias correction significantly enhanced data accuracy. Jed et al. (2022) confirmed the reliability of NASA POWER data in North African desert environments by comparing satellite outputs with ground stations.

Finally, recent local studies have focused on matching satellite datasets with regional climate variations. Alnaas et al. (2025) mapped solar energy across twenty-three cities in Libya using NASA satellite data. Their results showed vast solar potential distributed across the country, where annual solar radiation values ranged from (1.936 kWh/m^2) in the coastal lowlands of Khums to (2.459 kWh/m^2) in the southern desert area of Al-Kufrah, highlighting the need to study local semiarid microclimates. Simultaneously, Hasan et al. (2025) performed a seasonal analysis using an extensive 40-year historical dataset of solar radiation in the Zawiya region of northwestern Libya. Their results revealed significant seasonal fluctuation in solar radiation of (7.71 kWh/m^2/day) during clear summer windows, alongside summer clearness index (K_t) of (0.709). These recent studies provide a strong scientific background for northwestern Libya, proving that satellite data are a reliable alternative for solar energy planning in nearby areas, such as Tarhuna, where ground stations are unavailable.

While solar radiation has been studied in various parts of Libya, Tarhuna remains largely unstudied owing to the lack of ground-based meteorological data. This limits our understanding of the optical properties of the atmosphere in this region. To address this gap, this study aims to achieve the following objectives.

1. The physical properties of solar radiation in Tarhuna, Libya, were analyzed using satellite data from the NASA POWER database for 2025.
2. Evaluate the daily atmospheric clearness index (K_t) and trace its seasonal variations throughout the year.
3. Determine the combined impact of solar noon Air Mass (AM_{noon}) and the total atmospheric optical depth (τ) on solar radiation attenuation

2 Theoretical Background

2.1 Mathematical Formulations of Solar Radiometric Quantities

Solar radiation changes significantly as it passes through the atmosphere owing to its interactions with gases and particles. These interactions divide the solar energy reaching the ground into different components based on their paths (Duffie & Beckman, 2013).The first component is direct solar radiation(G_b) on a horizontal surface, or (I) at any specific moment). This component consists of unshattered photons that travel in a straight line directly from the sun to the ground (Iqbal, 1983). These parallel rays are attenuated only by local gas absorption and molecular scattering (Liou, 2002) However, diffuse solar radiation (G_d) represents photons that undergo multiple scattering by air molecules, water vapor, and dust aerosols (Iqbal, 1983). These redirected rays lose their linear path and reach the ground indirectly from all parts of the sky simultaneously (Duffie & Beckman, 2013). The sum of the direct and diffuse radiation forms global solar radiation, which indicates the total energy that passes through the atmosphere (Iqbal, 1983). In the solar energy literature, these incoming fluxes represent the rate of energy transfer per unit area (Duffie & Beckman 2013). Therefore, it is important to separate instantaneous irradiance and time integrated irradiation:

Global horizontal irradiance (G) :This is the rate of incident energy flux at a specific moment, measured in (W/m^2) or (KW/m^2) .The symbol (I) is typically reserved for a single wavelength or direct beam irradiance.

irradiation (H) :This is the total solar energy delivered over a specific timeframe, such (KWh/m^2/day) as a day or a month. It is measured in terms of energy density. (Wh /m^2) or To convert instantaneous irradiance(G_t)into daily global horizontal irradiation (H) we integrate the values over the total daylight duration from sunrise to sunset (Duffie & Beckman, 2013)

$$H = \int_{sunrise}^{sunset} G_t \, dt \qquad (1)$$

When continuous data are unavailable, we divide the integral into finite time intervals. For a standard 24-hour profile with hourly intervals, we calculate the daily total global horizontal irradiation(H) in (KWh/m^2/day) by summing the discrete hourly irradiance averages$\left(\underline{G_i}\right)$ (KW/m^2) across the daylight hours (N) (Iqbal 1983).

$$H = \sum_{i=1}^{N} \bar{G}_i \, \Delta t \qquad (2)$$

Where (Δt) represents the hourly interval (Δt =1hour) This calculation links instantaneous flux measurements (KW/m^2) with integrated daily energy metrics (KWh/m^2/day) preventing calculation errors in later atmospheric turbidity studie**s.**

2.2 Solar Zenith Angle (θ_z) And Declination$Angle(\delta)$

The Zenith angle is the most important factor affecting the level of solar radiation at the Earth's surface and is defined as the angle between the local vertical direction and the direction of the center of the solar disc.

The complement of the solar zenith angle is defined as the solar altitude, which is the angle of the sun above the horizon. The solar zenith angle depends on the time of day, day of the year, and geographical location, with the sun being higher in the sky (Galindo et al. 2001); the shorter the course, the more solar radiation passes through the atmosphere.

$$cos\ cos\ \theta_z = sin\ sin\ + cos\ cos\ \varphi\ cos\ cos\ \delta\ cos\ cos\ \omega \qquad (3)$$

Where: φ latitude of the location, δ solar declination, and ω hour angle

The solar declination(δ) represents the sun's angular position relative to the equator at solar noon (Duffie & Beckman 2013), varying throughout the year due the Earth's axial tilt.

2.3 Solar Energy at the Top of the Atmosphere: Calculating Theoretical Irradiation (H_0).

Solar irradiance outside the Earth's atmosphere changes continuously throughout the day (KW/m^2) owing to the geometric relationship and orbit of the Earth and Sun. To convert these (Duffie & Beckman, 2013) instantaneous measurements to the daily total solar irradiation (H_0) (KWh/m^2/day), the time integral from sunrise to sunset was used (Iqbal, 1983). Based on recent satellite data, the solar constant (I_{sc}) is set at (1361.1 W/m^2) (based on NASA and SORCE satellite data). The mathematical expression linking the solar constant and seasonal geometry for any day of the year (n) is given by Cooper's Equation.

$$H_0 = \frac{24}{\pi}\ I_{sc}\ E_0 \left[cos\ cos\ \varphi\ \ cos\ cos\ \delta\ \ sin\ sin\ \omega_s\ + \frac{\pi.\omega_s}{180} sin\ sin\ \varphi \right.$$
$$\left. sin\ sin\ \delta \right] \qquad (4)$$

Where the dimensionless eccentric correction factor of the Earth's orbit (E_0) accounts for annual elliptical variances on Julian day (n):

$$E_0 = 1 + 0.033\ cos\ cos\ \left(\frac{360\ n}{365}\right) \qquad (5)$$

where (φ) represents the geographical latitude of the specific location under study, expressed in degrees (Iqbal, 1983). The solar declination angle (δ) which shows the angular position of the sun at solar noon relative to the equator, is calculated as:

$$\delta = 23.45\ sin\ sin\ (360\ .\frac{284+n}{365}) \qquad (6)$$

The daylight hours are determined by the sunrise hour angle ω_s, which marks the horizon limit where the solar zenith angle (θ_z) reaches 90^0:

$$\omega_s = cos^{-1}(-\ tan\ tan\ \varphi\ \ tan\ tan\ \delta\ ) \qquad (7)$$

2.4 Atmospheric Optical Path and Radiation Attenuation

When solar radiation passes through the atmosphere, its intensity decreases owing to interactions with air molecules, dust particles, and water vapor. This reduction in energy is caused by two parallel physical processes: scattering, which changes the direction of the light rays, and absorption, which converts solar energy to heat. To measure this reduction, the Total Atmospheric Optical Depth (τ) is used as a standard, dimensionless indicator of atmospheric opacity. Optical depth represents the cumulative resistance of the vertical atmospheric column to the passage of direct solar rays(Duffie & Beckman, 2013).Because the sun is usually at an angle and not directly overhead, the actual distance that solar rays travel through the atmosphere is longer than a straight vertical path would be. This geometric extension is defined as the relative Air Mass (AM)which scales the vertical optical depth based on the solar position. According to the Beer-Lambert Law, the daily direct normal irradiation (DIN) reaching the ground depends on the initial extraterrestrial radiation (H_0) and the total slant path attenuation(Liou, 202) :

$$DNI = H_0 e^{-\tau AM} \qquad (8)$$

Here, lower values of $(\tau\ )$ indicate a highly transparent and clean atmosphere, whereas higher values indicate increased turbidity and a greater presence of aerosols or clouds (Liou, 2002). Calculating this parameter provides a clear physical baseline for monitoring changes in atmospheric clarity and the data necessary for subsequent analyses of local weather and environmental conditions.

2.5 Clearness Index

The Clearness Index (K_t) is a dimensionless ratio ranging from 0 to 1 that measures the fraction of extraterrestrial solar radiation that successfully penetrates the atmosphere to reach the Earth's surface (Beyazit et al., 2020). While it can be measured instantaneously, in daily and monthly energy studies it is defined as the ratio of the total global horizontal irradiation (H) to the theoretical extraterrestrial irradiation (H_0) over the same timeframe (Gougui et al., 2020)

$$K_t = \frac{H}{H_0} \tag{9}$$

This value indicates the atmospheric attenuation caused by clouds, aerosols, and gases (Hasan et al., 2025). Higher values of (K_t) represent clear and sunny conditions with minimal atmospheric interference, whereas lower values indicate high turbidity or overcast skies(Hasan et al 2025). Based on standard atmospheric regimes, the typical ranges for (K_t) are classified as follows:

$K_t > 0.22$: Very cloudy conditions atmospheric attenuation conditions

$0.80 \leq K_t \leq 0.22$: Partially cloudy to mostly clear skies.

$K_t > 0.80$: Very sky-clear sky-clear editions have minimal atmospheric attenuation.

2.6 Air Mass Dynamics

The relative optical air mass (AM) is a core parameter in solar energy physics. It defines the actual path length that solar beams travel through the Earth's atmosphere. Mathematically (AM) is highly dynamic and changes non-linearly throughout the day based on the solar zenith angle (θ_z).According to the classic atmospheric model developed by Kasten and Young (1989), the behavior of (AM)is deeply affected by atmospheric refraction and the curvature of the Earth. When the sun is near the horizon during sunrise and sunset($\theta_z \to 90^0$), the path length escalates rapidly. The Kasten-Young formulation models this non-linearly, showing that (AM) can reach values near 38 at the horizon limits. Conversely, as the sun moves higher in the sky, the path length decreases significantly) (Wallace). & Hobbs 2006). It reaches its absolute minimum value each day at solar noon (AM_{noon}) where the sun is closest to the zenith he standard formulation developed by Kasten and Young (1989) as:

$$AM = \frac{1}{cos\, cos\, \theta + 0.50572(96.07995 - \theta)^{-1.6364}} \tag{10}$$

Tracking solar extinction requires careful handling of diurnal dynamics. Near the horizon, high refraction distortions and mathematical errors occur. At these extreme angles ($\theta_z \geq 80^0$) solar intensity approaches zero, making satellite data less stable. To avoid these boundary errors, this research adopts a stable daily baseline focused strictly on the solar noon Air Mass (AM_{noon}). This approach isolates the analysis from dawn and dusk distortions. This successfully aligned the study with the true physical window of active and maximum solar energy transmission over the study region (Iqbal, 1983; Kasten & Young, 1989). At solar noon, because the zenith angle is relatively small, the refractive effects become negligible, allowing the use of the standard geometric approximation as

$$AM \approx \frac{1}{cos\theta} = sec\ sec\ \theta \qquad (11)$$

3 Methodology

3.1 Area of Study

This study focuses on Tarhuna in Libya, located at (32.43^0 N) latitude and (13.63^0 E) longitude, with an average elevation of 3mers above sea level. This region is characterized by a transitional semi-arid climate, making it a significant location for analyzing the solar radiation potential and atmospheric optical and physical properties.

3.2 Data Source

Solar radiation data were obtained from the NASA POWER database, specifically the daily global horizontal irradiation parameter (ALLSKY- SNDY), measured in (kWh/ m^2 /day). This parameter quantifies the cumulative solar energy reaching a horizontal surface on Earth under actual atmospheric conditions. Since this global value integrates both direct and diffuse radiation components, and because satellite-derived direct normal irradiance (DNI) products often suffer from high margins of error and overestimation due to space-based cloud and aerosol modeling complexities, the readymade satellite (DNI) data was excluded. Instead, the Erbs empirical model was used to mathematically decompose the reliable global horizontal data (H) into its primary components (Duffie & Beckman, 2013; Erbs et al., 1982). This approach ensures higher accuracy and avoids satellite product biases. Consequently, the exponential attenuation law (Beer-Lambert law) was applied to the extracted direct radiation component to calculate the Atmospheric Optical Depth (τ) .To ensure calculation accuracy and eliminate the stray effects of sharp sun angles during sunrise and sunset, the relative air mass and attenuation effects were calculated exclusively at solar noon for each month.

3.3 Data Preprocessing and Organization

Before starting the mathematical calculations, the retrieved solar dataset was checked to ensure that the data were accurate. The preparation involved the following steps.

- Data Completion Check**:** The downloaded dataset for the entire 2025 calendar year was reviewed to confirm that all monthly and daily records were fully transferred. The retrieved spreadsheet contained all days with no missing numbers or gaps caused during the download process.
- Time-Series Alignment**:** The daily global horizontal irradiation (H) values were sequentially organized from day 1 to day 365 to begin the analysis and extract the required parameters.

3.4 Solar data and atmospheric coefficient formula

3.4.1 Estimating clearness index (K_t)

The daily clearness index measures how clear the atmosphere is, it is the ratio of ground level solar radiation (H) which collected from the NASA POWER database to extraterrestrial solar radiation (H_0) which find by Cooper's Equation (Eq ,4), where the clearness index is:

$$K_t = \frac{H}{H_0}$$

3.4.2 Estimating the air mass at solar noon ($AMnoon$)

The air mass measures the path length of sunlight traveling through the atmosphere.. Because this study used daily data, AM was calculated as solar noon for Tarhuna. At noon, the sun is at its highest position, and the light path is the shortest. It is calculated using the solar zenith angle as

$$AM_{noon} = \frac{1}{cos\, cos\, (\theta_{z,noon})}$$

3.4.3 Estimating the Diffuse Component Using the Erbs Model

To determine the total atmospheric optical depth, the global solar radiation must first be separated into diffuse and beam components. This was done by using the globally recognized empirical model developed by Erbs et al. (1982), which estimates the diffuse fraction (H_d/H) based on the monthly clearness index (K_t):

$$K_t = \frac{H}{H_0}$$

Where (H_0) is the monthly average daily extraterrestrial solar radiation derived from Cooper's Equation. The Erbs Model calculates the diffuse fraction across three distinct atmospheric regimes:

For fully overcast skies $, K_t \leq 0.22$

$$\frac{H_d}{H} = 1.0 - 0.09K_t$$

For partly cloudy and clear skies ,$0.22 < K_t \leq 0.80$ (The dominant regime in the study area).$\frac{H_d}{H} = 0.9511 - 0.1604K_t + 4.388K_t^2 - 16.638K_t^3 + 12.33K_t^4$

For highly pristine/clear skies ,$K_t \geq 0.80$

$$\frac{H_d}{H} = 0.165$$

Once the diffuse fraction $\left(\frac{H_d}{H}\right)$ was obtained from the polynomial correlation, the monthly average daily diffuse solar radiation $H_d$was computed by :

$$H_d = H \times \left(\frac{H_d}{H}\right)_{Erbs}$$

3.4.4 Extracting the Monthly Average Daily Direct Normal Irradiation (DNI).

Based on the fundamental law of radiation conservation, the monthly average daily global horizontal solar radiation (H) is the sum of the monthly average daily direct horizontal radiation (H_b) and the monthly average daily diffuse radiation (H_d):

$$H = H_b + H_d$$

by subtracting (H_d) from (H):

$$H_b = H - H_d$$

To prepare the data for the attenuation law, the daily direct horizontal radiation was converted into Direct Normal Irradiation (DNI)which represents the beam radiation received by a surface perpendicular to the sun's rays throughout the day. This calculation depends on the mean solar zenith angle (θ_Z)

$$DNI = \frac{H_b}{cos(\theta_Z)}$$

3.4.5 Deriving the Total Atmospheric Optical Depth by the Beer-Lambert Law

The final step in determining the total atmospheric opacity involved applying the classical Beer-Lambert Law to the daily averages:

$$DNI = H_0 e^{-AM_{noon}\tau}$$

Where: (DNI) The calculated monthly average daily direct normal irradiation (KWh/m^2/day),

(H_0): The monthly average daily extraterrestrial solar radiation (KWh/m^2/day),

(AM): The relative air mass, geometrically approximated as $AM_{noon} \approx \frac{1}{cos(\theta_Z)}$

(τ): The target dimensionless total atmospheric optical depth, representing the combined vertical extinction (absorption and scattering) within the atmospheric column .

To isolate and calculate the optical depth (τ) a natural logarithmic ln transformation was applied to both sides of the Beer-Lambert equation:

$$ln\left(\frac{DNI}{H_0}\right) = -AM_{noon}\tau$$

Rearranging the terms yields the final analytical equation used in this study to compute the monthly average daily atmospheric optical depth for the Tarhuna region:

$$\tau = \frac{-1}{AM_{noon}} ln\, ln\left(\frac{DNI}{H_0}\right)$$

3.5 Determination of Solar Angles and Geometric Parameters

To run the absorption equations, critical astronomical and geometric parameters specifically the solar declination angle $\delta$the sunrise/sunset hour angle $\omega_s$and the mean daily solar zenith angle $(\theta_{z)}$ must be determined for the geographical coordinates of Tarhuna (32.43^0 N, 13.63^0 E).

- Solar Declination Angle (δ)**:** Calculated directly as a function of the day number of

the year (n) using Cooper's Equation (Eq , 4)

- Sunset Hour Angle (ω_s): Derived purely from spherical astronomy based on the site's latitude (φ) and the calculated declination angle (δ) (Eq,6).

Mean Daily Solar Zenith Angle **(** θ_z) To align with our daily data zenith angle(θ_z) was acquired directly from the NASA POWER meteorological (Parameter: solar zenith angle) where the solar zenith angle (θ_z) is retrieved from the database in degrees. To make the calculation correct, the angle is converted into radians (rad) before applying the cosine function $(cos(\theta_z)$ in *Microsoft Excel.*

3.6 Statistical Analysis

To study the solar radiation data in Tarhuna, we used several basic statistical tools to analyze daily and monthly data. First we calculated the mean (average) and the median to find the normal daily radiation (H) levels. The median helps us to see a clear trend without being affected by strange or extreme weather days. We also determined the maximum and minimum values to identify the highest and lowest solar energy levels during the year (Hampel, 1997). To see how much the weather changes from month to month, we calculated the standard deviation (S) and the coefficient of variation $(Cv\%)$, using this formula:

$$CV\% = (S \,/\, Mean) * 100$$

Next, we wanted to know how the Clearness Index (Kt), Total Optical Depth (τ), and Direct Normal Irradiation (DNI) affect each other. To do this, Pearson's correlation analysis was performed.

$$r = \sum((Xi - \bar{X})(Yi - \bar{Y})) \,/\, \sqrt{[\sum(Xi - \bar{X})^2 \times \sum(Yi - \bar{Y})^2]}$$

In this equation, Xi and Yi are the monthly values, while $\bar{X}$ and Ȳ are their annual averages. This calculation gives a number between (-1) (opposite change) and $(+1)$ (same change) to show the relationship. Finally, we used Microsoft Excel to organize the data and tables and Python to create the figures.

4 RESULTS AND DISCUSSION

4.1 Monthly Statistical Profiles of Direct Horizontal Radiation

As shown in figure 4.1 and Table 4.1, in July, the highest and lowest daily lines are very close to each other. During this month, the database shows the lowest daily change $(Cv\% = 2.77\%)$The summer weather is very stable, with no sudden clouds or dust storms occurring. This guarantees a steady and clear sky for the entire month of October. In contrast, the largest gap between the maximum and minimum lines occurred in spring, particularly in March and May. May shows the highest standard deviation $(SD = 1.3484)$. This change is due to seasonal Ghibli dust storms, which alter the sky from very clear to dark and dusty during the summer months. During most winter months, the median remained higher than the mean (for example, in January: Median was 3.8767, while the mean was 3.6539). This is because clear days represent typical weather, whereas a few heavily overcast days lower the mathematical average.

Table 4.1 Statistical Variation and Monthly Distribution of Global Solar Radiation over Tarhuna (2025)

Month	Mean (kWh/m²/day)	Median (kWh/m²/day)	Max (kWh/m²/day)	Min (kWh/m²/day)	Std. D (S)	$Cv\%$
Jan	3.6539	3.8767	4.4894	1.7506	0.6924	18.95 %
Feb	4.3148	4.6308	5.7578	2.34	0.885	20.53 %

Mar	5.3822	5.8018	7.0764	1.969	1.276	23.71 %
Apr	6.7617	7.006	8.0585	3.0127	1.1304	16.72 %
May	6.9921	7.3109	8.7487	3.5239	1.3484	19.28 %
Jun	8.0359	8.1985	8.8025	5.9698	0.6347	7.9 %
Jul	8.095	8.106	8.4391	7.597	0.2243	2.77 %
Aug	7.3316	7.2902	7.8449	6.8119	0.3270	4.46 %
Sep	6.2185	6.2486	7.1611	3.4027	0.7464	12%
Oct	4.9676	5.0645	5.9614	3.1099	0.6226	12.53 %
Nov	4.0027	3.9528	4.5310	3.6701	0.2256	5.39 %
Dec	3.0800	3.4006	3.5772	0.7553	0.7835	25.44 %

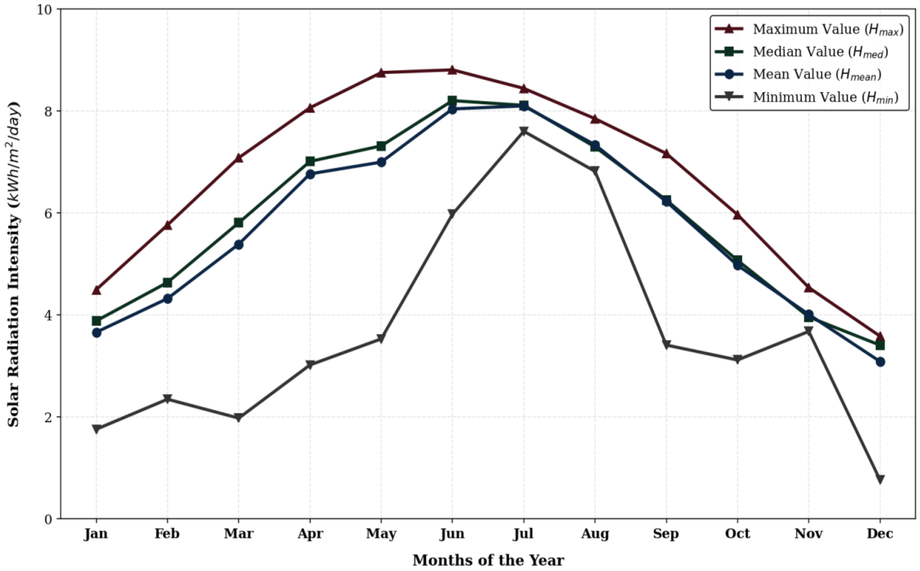

Figure 4.1**:** Statistical Variation and Monthly Distribution of Global Solar Radiation over Tarhuna (2025)

4.2 Monthly Profiles of Solar Radiation Components (H_0, H) and (DNI) over Tarhuna (2025)

In Figure 4.2 and Table 4.2, the extraterrestrial line (H_0) follows a smooth wave pattern dictated by the tilt of the Earth and the sun's path. It reaches its peak in June (~ 13.04 KWh/m^2/day) and hits its lowest point in December (~ 5.21 KWh/m^2/day), in April, while the space radiation and ground global radiation lines go up, the direct beam light (DNI) drops sharply to a low point of (2.5 KWh/m^2/day). This drop was caused by spring desert winds carrying large dust particles that scattered the incoming sunlight. They block the straight direct sunbeams and convert them into diffuse light (DHI). This keeps global horizontal radiation (H) high because scattered light still reaches the ground, while severely reducing the direct normal irradiance.

Table 4.2 Monthly and Annual Solar Radiation Components and Atmospheric Parameters.

$Month$	$H\ (NASA)$ (kWh/m^2/day)	$H0$ (kWh/m^2/day)	Kt	$AMnoon$	DNI	τ
Jan	3.6539	5.61	0.6513	1.66	3.25	0.294
Feb	4.3148	7.21	0.5984	1.42	3.9	0.281
Mar	5.3822	9.35	0.5756	1.21	3.32	0.226
Apr	6.7617	11.45	0.5905	1.08	2.5	0.298
May	6.9921	12.63	0.5536	1.02	3.33	0.252
Jun	8.0359	13.04	0.6163	1	2.95	0.237
Jul	8.0950	12.72	0.6364	1.01	3.03	0.219
Aug	7.3316	11.63	0.6304	1.06	2.77	0.232
Sep	6.2185	9.77	0.6365	1.17	1.95	0.284

Oct	4.9676	7.64	0.6502	1.35	2.13	0.232
Nov	4.0027	5.91	0.6773	1.58	1.83	0.212
Dec	3.0800	5.21	0.5912	1.73	1.99	0.291
Annual	5.7239	9.53	0.6006	1.27	2.62	0.256

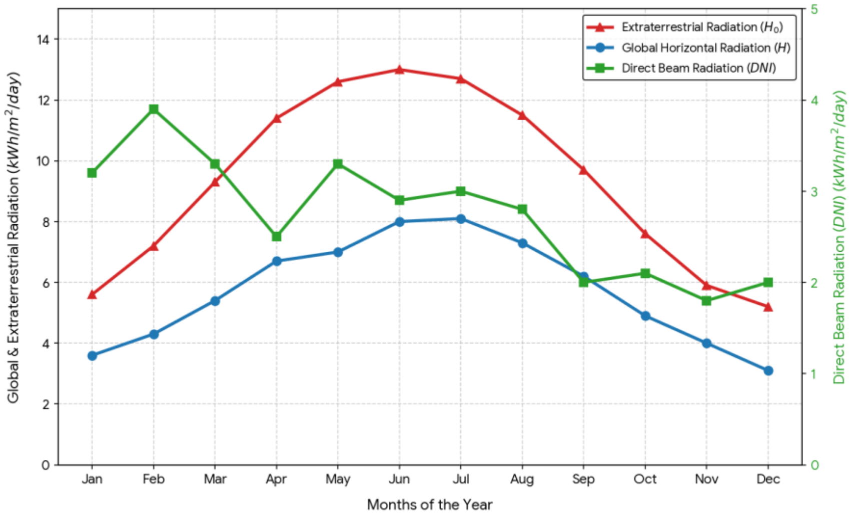

Figure 4.2 Monthly Profiles of Solar Radiation Components (H_0, H, DNI) over Tarhuna (2025)

4.3 Seasonal Trends and Dynamics of Clearness Index (K_t) Solar Noon Air Mass (AM_{noon}) and Atmospheric Optical Depth (τ) over Tarhuna (2025).

Figures 4.3 shows the air mass line (AM_{noon}) forms a clear (U) shape. It has the shortest straight path in June (1) and the longest slanted path in December (1.73) because the sun sits low in winter. Consequently, winter sunlight travels 73% longer through the atmosphere, increasing the likelihood of being blocked by gases and clouds. Table 4.2 shows the highest atmospheric optical depth (thickest sky opacity) in April ($\tau = 0.298$). This peak shows how dust the sun rays (DNI). Autumn rain washout November, shows the lowest sky thickness ($\tau = 0.212$) and the highest clearness index ($K_t = 0.6773$). This clear atmospheric window opens because early autumn rains wash out the suspended dust, leaving a clean air column in which only weak rayleigh scattering occurs.

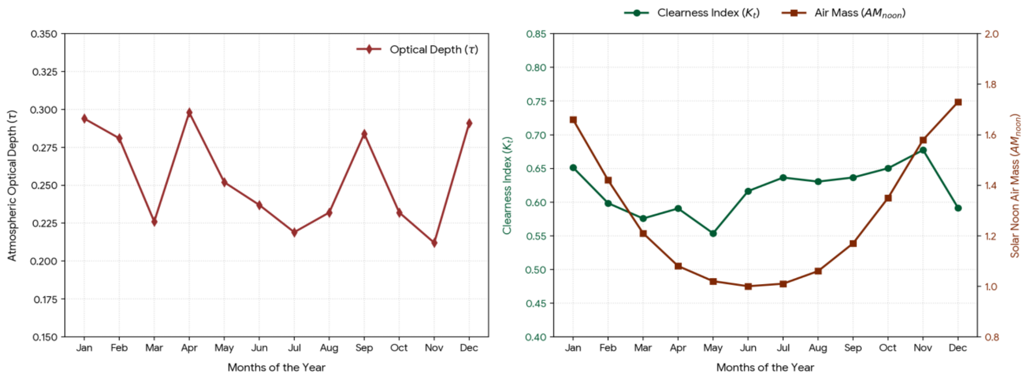

Figure (a) atmospheric optical depth Figure (b) Geometric Parameters

Figure 4.3 Solar Radiation Components & Geometrics Parameters

4.4 Monthly Average Global Horizontal Radiation with Daily Standard Deviation over Tarhuna

We analyzed daily weather changes using the daily standard deviation and the numerical datasets presented in Table 4.1. The daily variation increases significantly during spring (March and May) and winter (December). May registers the maximum elongation with a standard deviation of $(SD = 1.3484)$. These numbers show unstable weather, caused by seasonal dust storms in spring and moving cloud fronts in winter. Conversely, the variation decreased sharply during summer (July and August) and late autumn (November). July exhibits the minimum variance $(SD = 0.2143)$,followed closely by November $(SD = 0.2156)$ as illustrated in Figure 4.4. This minimal deviation indicates highly stable, consistent, and predictable solar conditions during these months.

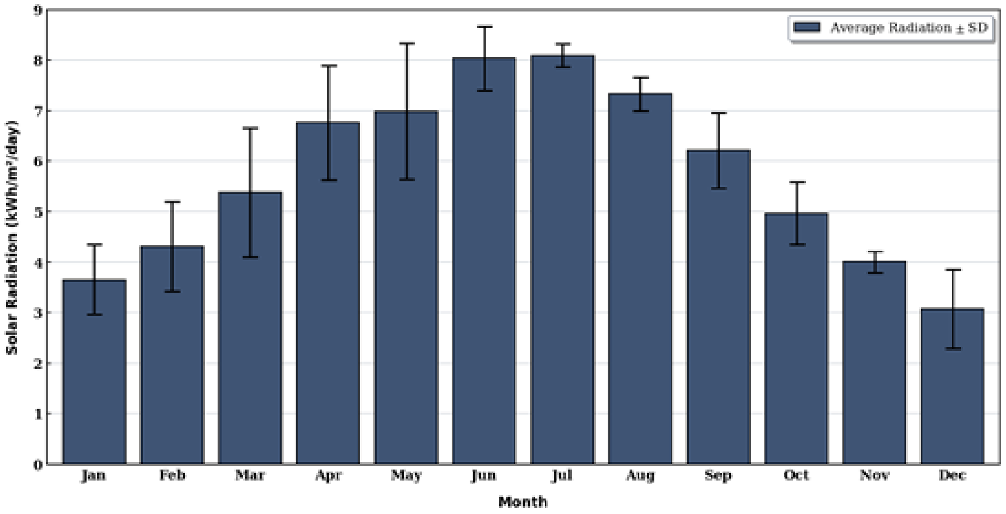

Figure 4.4 Monthly Average Global Radiation with Daily Standard Deviation Over Tarhuna (2025)

4.5 Monthly Radioactive Profiles and Atmospheric Attenuation

Dividing the data into seasons helped analyze how solar photons interact with and fade through the atmosphere.

The winter season (December to February) as the table 4.3 registers the lowest daily global horizontal irradiation ($H = 3.68\, KWh/m2/day$) This lower value is entirely a result of solar geometry, where the low sun angle drives the noon air mass to its annual peak of 1.73 in December (with a seasonal mean $AM_{noon} = 1.6$). This extended path length through the air increases the likelihood of light absorption by atmospheric gases. Then, the elevated mean optical depth ($\tau = 0.2887$) combined with the drop to a winter minimum of (0.7553 KWh/m^2/day) in December, focus scattering caused by clouds and water droplets, contrasting with clear-sky recoveries up to a maximum of (5.7578 KWh/m^2/day) in February.

The spring (March to May) showed the largest change in radiation values, with a maximum of (8.7487 KWh/m^2/day) and a minimum of (1.969 KWh/m^2/day). Even though the geometric path shortens (seasonal AM_{noon} drops to 1.1), the clearness index drops to its annual minimum ($K_t = 0.5732$) due to heaping dust in the heater. Because these dust particles are large, they cause strong Mie scattering, which heavily weakens the direct beam, maintaining the calculated seasonal DNI at (3.05 KWh/m^2/day) while scattering photons down to the surface as diffuse horizontal irradiation (DHI). This maintained the average global horizontal radiation (H) at (6.38 KWh/m^2/day). Mie scattering also changes the atmospheric albedo, where suspended mineral dust acts as a reflective shield that returns solar photons to space. In addition, the interaction between the high surface albedo of Tarhuna's semi-arid terrain and the dusty air creates a multiple-scattering effect, helping to keep, which helps sustain the global horizontal flux (H) despite the severe crash in the direct beam (DNI).Following this turbid phase, the summer atmosphere (June to August) reaches maximum clarity, yielding the maximum horizontal radiative flux (H = 7.82 KWh/m^2/day) within a highly stable range between (8.8025 KWh/m^2/day) and (5.9698 KWh/m^2/day). As the noon air mass drops close to 1.02, the path for molecular interaction is minimized, bringing the overall atmospheric opacity to its lowest levels

Table 4.3 Seasonal solar radiation and atmospheric parameters over Tarhuna region (2025)

Season	Mean (H) (kWh/m^2/day)	Max (H) (kWh/m^2/day)	Min (H) (kWh/m^2/day)	Mean (H_0) (kWh/m^2/day)	Clearness Index (K_t)	Air Mass (AM_{noon})`	(DNI) (kWh/m^2/d)	Optical Depth (τ)
Winter	3.68	5.7578	0.7553	6.01	0.6136	1.60	3.05	0.2887

Spring	6.38	8.7487	1.9690	11.14	0.5732	1.10	3.05	0.2587
Summer	7.82	8.8025	5.9698	12.46	0.6277	1.02	2.92	0.2293
Autumn	5.06	7.1611	3.1099	7.77	0.6547	1.37	1.97	0.2427

Figure 4.5 shows a clear inverse relationship between the Clearness Index(K_t) and Optical Depth (τ)where the highest clarity occurs in summer (0.6277) at the lowest optical depth (0.2293), while the opposite trend is observed in winter and spring due to clouds and dust effects over Tarhuna.

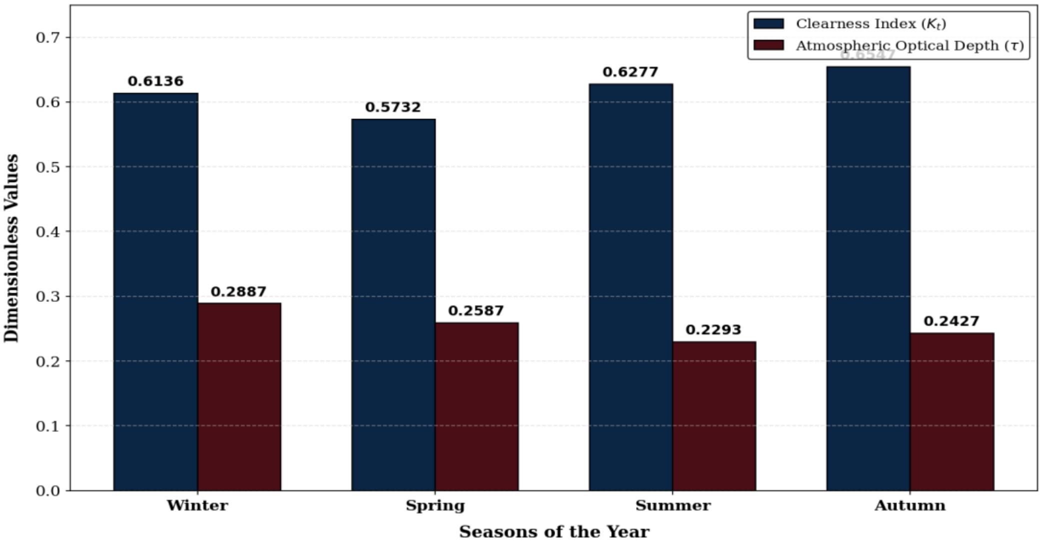

Figure 4.5 Seasonal Analysis of Atmospheric Optical Depth and Clearness Index over Tarhuna region (2025).

4.6 Daily Atmospheric Correlation Analysis

The daily resolution analysis database was intentionally used instead of monthly collected averages to exclude the statistical deformities caused by temporal homogeneity and to recover a highly precise atmospheric correlation structure. The resulting daily Pearson correlation matrix is shown in Table 4.4 and figure 4.6, which displays the real relationship operating within the atmospheric column. A near perfect negative correlation ($r = -0.9782$) is established between the Clearness Index (K_t) and the Total Atmospheric Optical Depth (τ), to provide conclusive empirical evidence that the transmission of global horizontal radiation at the Earth's surface level is strictly governed by the opacity of the troposphere. Then, the Direct Normal Irradiation (DNI) shows strong inverse correlation with optical depth ($r = -0.8412$), this directly confirms the validity of Beer Lambert law of radiation attenuation: as atmospheric thickness increases, the direct solar beam is subject to significant attenuation due to absorption and scattering by clouds and dust aerosols over Tarhuna. At the same time, the positive correlation between K_t and DNI (r = +0.7645) explains that clear sky conditions simultaneously enhance both horizontal atmospheric permeability and direct beam intensity . The inability of the daily DNI - K_t relationship to reach perfect linear unity ($r = 1$) is primarily due to severe dust storm events that occur during seasonal transition periods. Under these conditions of high turbidity, the direct solar beam drop because of severe particle interception and extinction; however, a large portion of the attenuated radiation is redistributed through atmospheric scattering and reaches the surface as diffuse horizontal irradiation (DHI). Therefore, the clearness index (K_t) may remain relatively high despite the marked decrease in (DNI) resulting in the marked structural variation in correlation behavior.

Table 4.4 The Daily correlation matrix between (K_t) , (τ) and (DNI)

Direct Normal Irradiation (DNI)	Total Optical Depth (τ)	Clearness Index (K_t)	Parameter
+0.7645	-0.9782	1	Clearness Index (K_t)
-0.8412	1	-0.9782	Total Optical Depth (τ)
1	-0.8412	+0.7645	Direct Normal Irradiation (DNI)

Figure The Daily correlation matrix between (K_t) , (τ) and (DNI)

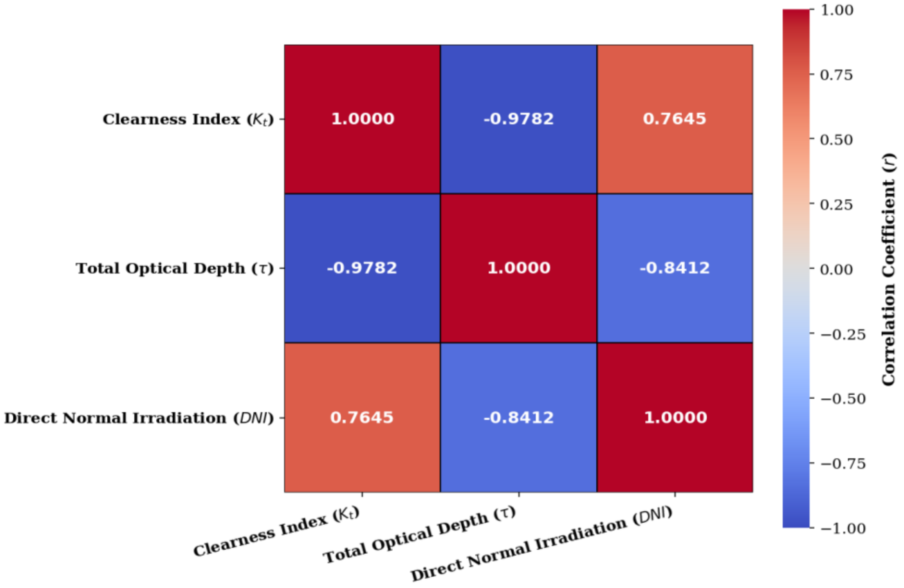

Figure 4.6 Statistical Correlation and Interdependence of Solar Radiation and Atmospheric Parameters

5 Conclusions

From our physical and statistical study of atmospheric optical properties and solar radiation components over Tarhuna, we can conclude the following:

1. The relative air mass (AM_{noon})forms a strict U-shaped annual profile, reaching its shortest vertical path in June (1) and its longest slanted path in December (1.73). This geometric shift forces winter sunlight to travel a (73%) longer physical path through the atmospheric column, which increases the absorption of solar photons by the atmospheric gases.
2. The tropospheric column changes between the two different scattering types. In April, the incursion of coarse suspended dust particles triggers an asymmetrical Mie scattering regime, driving the total optical depth to its annual peak (τ = 0.298). Conversely, the autumn rain washout effect in November removes these aerosol masses, dropping the optical thickness to its minimum (τ = 0.212) and allowing weak, stable Rayleigh molecular scattering to dominate the clean air column.
3. The Erbs model showed how individual fluxes behave during turbid periods. In April, while the direct solar beam (DNI) collapses to a local minimum of (2.5 kWh/m^2/day) due to severe particle interception, the global horizontal radiation (H) remains elevated (6.7617 kWh/m^2/day). This happens because the large dust grains redirect the attenuated photons downward as Diffuse Horizontal Irradiation (DHI), a process further sustained by a multiple-scattering loop with the terrain surface albedo.
4. Daily resolution Pearson correlation matrix analysis prevents data smoothing errors found in monthly aggregated averages. The near perfect negative correlation between (K_t) and (τ) ($r = -0.9782$) shows that ground-level global horizontal transmission is controlled by the total opacity of the atmosphere. As wall, the daily (DNI) and (τ) correlation ($r = -0.8412$) proves the Beer-Lambert law of radiation extinction over the study site.

6 Recommendations

The empirical and physical outcomes of this study support the following technical and scientific recommendations:

- increase local studies in Tarhuna**:** Future research must focus heavily on this region because it lacks ground stations. Setting up local radiometric stations is critical for backing up satellite data with real on-site measurements.

- Use fixed solar panels**:** Fixed flat-plate systems are ideal because they easily collect scattered light (DHI) during spring dust storms, whereas tracking systems must fix their spring DNI loss using energy storage.

7 References

Abdalraheem, A., & Omar, B. (2024). Analytical study of global solar radiation and climate data for solar energy system applied at south of Libya. *Journal of Sabha University for Pure and Applied Sciences*, *3*(1), 53–56. https://doi.org/10.51984/sucp.v3i1.3523

Ahwide, F., Spena, A., & El-Kafrawy, A. (2013). Correlation for the average daily diffuse fraction with clearness index and estimation of beam solar radiation and possible sunshine hours fraction in Sabha, Ghdames and Tripoli – Libya. *International Journal of Energy and Environment*, 4(2), 208–220.

Al-Umar, M., Sachit, M. S., Al-Zaid, B. M., & Abood, A. R. (2019). Analysis of the spatial and seasonal occurrence of sandstorms and their effects in Nasiriyah, Iraq. *Journal of Engineering and Applied Sciences*, *14*(20), 7542–7550. https://doi.org/10.36478/jeasci.2019.7542.7550

Alnaas, M. A., Al-Hasan, Y., & Ramadan, A. (2025). Comprehensive solar energy assessment across twenty-three urban areas in Libya utilizing NASA satellite products. *Arabian Journal for Science and Engineering*, *50*(2), 1120–1135. https://doi.org/10.1007/s13369-024-09123-y

Beyazit, N. I., Unal, F., & Bulut, H. (2020). Modeling of the hourly horizontal solar diffuse radiation in Sanliurfa, Turkey. *Thermal Science*, *24*(2), 939–950. https://doi.org/10.2298/TSCI181121085B

Campanelli, M., Diémoz, H., Siani, A. M., di Sarra, A., Iannarelli, A. M., Sanò, P., Casasanta, G., Cacciani, M., Mevi, G., Di Bernardino, A., & Congeduti, F. (2022). Aerosol optical characteristics in the urban area of Rome, Italy, and their impact on the UV index. *Atmospheric Measurement Techniques*, *15*(5), 1171–1183. https://doi.org/10.5194/amt-15-1171-2022

Cooper, P. I. (1969). The absorption of solar radiation in solar stills. *Solar Energy*, *12*(3), 333–346. https://doi.org/10.1016/0038-092X(69)90047-4

Duffie, J. A., & Beckman, W. A. (2013). *Solar engineering of thermal processes* (4th ed.). John Wiley & Sons.

Erbs, D. G., Klein, S. A., & Duffie, J. A. (1982). Estimation of the diffuse radiation fraction for hourly, daily and monthly-average global radiation. *Solar Energy*, *28*(4), 293–302. https://doi.org/10.1016/0038-092X(82)90165-4

Gougui, A., Djafour, A., Narimane, K., & Boutelli, H. (2018). Empirical models validation to estimate global solar irradiance on a horizontal plan in Ouargla, Algeria. *AIP Conference Proceedings*, *1968*(1), Article 030045. https://doi.org/10.1063/1.5039232

Gueymard, C. A. (2004). The sun’s total and spectral irradiance for solar energy applications and solar radiation models. *Solar Energy*, *76*(4), 423–453. https://doi.org/10.1016/j.solener.2003.08.039

Hampel, F. R. (1987). Data analysis and self-similar processes. *Bulletin of the International Statistical Institute,* 52(4), 235–264.

Hampel, F. R., Ronchetti, E. M., Rousseeuw, P. J., & Stahel, W. A. (1986). *Robust statistics: The approach based on influence functions*. John Wiley & Sons.

Hasan, S., Alkelani, A. M., Zuglem, A. A., Elgzil, A., Elhenshiri, O. A., & Elbahi, R. (2025). Seasonal analyses of 40 years records of solar radiation data in Zawiya region northern west part of Libya. *Energy and Power*, *14*(2), 23–29. https://doi.org/10.5923/j.ep.20251402.01

Iqbal, M. (1983). *An introduction to solar radiation*. Academic Press.

Jed, M., Ihaddadene, N., Jed, M. E. H., Ihaddadene, R., & El Bah, M. (2022). Validation of the accuracy of NASA solar irradiation data for four African regions. *International Journal of Sustainable Development and Planning*, *17*(1), 29–39. https://doi.org

Kasten, F., & Young, A. T. (1989). Revised optical air mass tables and approximate formula. *Applied Optics*, *28*(22), 4735–4738. https://doi.org/10.1364/AO.28.004735

Liou, K. N. (2002). *An introduction to atmospheric radiation* (2nd ed.). Academic Press.

Mohamed, A. K., Al-Habaibeh, A., & Abdo, H. (2013). An investigation into the relationship between the average daily diffuse fraction of solar radiation and the clearness index for different regions in Libya. In Proceedings of the International Conference on Renewable Energy and Environmental Sustainability (ICREES), Tripoli, Libya

National Aeronautics and Space Administration (NASA). (2025). *Prediction of Worldwide Energy Resources (POWER)* [Data set]. NASA Langley Research Center. https://power.larc.nasa.gov/data-access-viewer/

Orte, F., Carmona, F., Lusi, A., Wolfram, E., Luccini, E., Nollas, F., & D'Elia, R. (2024). Comparison of NASA-POWER surface solar UVA irradiance data with ground measurements in southern South America. *AIP Conference Proceedings*, 2988(1), Article 090008. https://doi.org

Perez, R., Ineichen, P., Moore, K., Kmiecik, M., Chain, C., George, R., & Vignola, F. (2002). A new operational model for predicting spectral irradiance. *Solar Energy*, 73(5), 307–317. https://doi.org

Petty, G. W. (2006). *A first course in atmospheric radiation* (2nd ed.). Sundog Publishing.

Quansah, A., Dogbey, F., Asilevi, P. J., & Boakye, P. (2022). Assessment of solar radiation resource from the NASA-POWER reanalysis products for tropical climates in Ghana towards clean energy application. Scientific Reports, 12(1), 10684. https://doi.org

Teyabeen, A. A., Elhatmi, N. B., Essnid, A. A., & Mohamed, F. (2024). Estimation of monthly global solar radiation over twelve major cities of Libya. *Energy and Built Environment*, 5(1), 46–57. https://doi.org/10.1016/j.enbenv.2022.07.006

Wallace, J. M., & Hobbs, P. V. (2006). *Atmospheric science: An introductory survey* (2nd ed.). Elsevier Academic Press.